Bulletin of the Seismological Society of America, Vol. 100, No. 2, pp. 640–656, April 2010, doi: 10.1785/0120090198

A Crust and Upper-Mantle Model of Eurasia and North Africa for *Pn* Travel-Time Calculation

by Stephen C. Myers, Michael L. Begnaud, Sanford Ballard, Michael E. Pasyanos, W. Scott Phillips, Abelardo L. Ramirez, Michael S. Antolik, Kevin D. Hutchenson, John J. Dwyer, Charlotte A. Rowe, and Gregory S. Wagner

Abstract We develop a regional seismic travel-time (RSTT) model and method for use in routine seismic analysis. The model parameterization is a global tessellation of nodes with a velocity profile at each node. Interpolation of the velocity profiles generates a 3D crust and laterally variable upper-mantle velocity. The upper-mantle velocity profile at each node is represented as a linear velocity gradient, which enables travel-time computation in approximately 1 millisecond. This computational speed allows the model to be used in routine analyses in operational monitoring systems. We refine the model using a tomographic formulation that adjusts the average crustal velocity, mantle velocity at the Moho, and the mantle velocity gradient at each node. While the RSTT model is inherently global, our first RSTT tomographic effort covers Eurasia and North Africa, where we have compiled a data set of approximately 600,000 *Pn* arrivals. Ten percent of the data set is randomly selected and set aside for testing purposes. Travel-time residual variance for the validation data is reduced by 32%. Based on a geographically distributed set of validation events with epicenter accuracy of 5 km or better, epicenter error using 16 *Pn* arrivals is reduced by 46% from 17.3 km (ak135 model) to 9.3 km (RSTT model) after tomography. The median uncertainty ellipse area is reduced by 68% from 3070 km^2 (ak135) to 994 km^2 (RSTT), and the number of ellipses with area less than 1000 km^2, which is the area allowed for onsite inspection under the Comprehensive Nuclear Test Ban Treaty, is increased from 0% (ak135) to 51% (RSTT).

Introduction

Event location accuracy is vitally important to seismic monitoring because the location itself can provide insight about the event, and subsequent analysis (seismic and nonseismic) relies on an accurate location. Efforts to reduce magnitude thresholds in global monitoring systems have prompted the inclusion of regional seismic data into routine analysis. Regional seismic phases, broadly defined as the dominant phases at event–station distances less than 2000 km, work toward lowering thresholds because these phases are recorded more reliably than the teleseismic phases that are traditionally used for global monitoring. Unfortunately, the current practice in monitoring systems of using a one-dimensional (1D, radially symmetric) Earth model as the primary means of computing travel times diminishes the utility of regional data because prediction of regional travel times with a 1D model is far less accurate than prediction of teleseismic travel times (e.g., Kennett *et al.*, 1995; Yang *et al.*, 2004; Flanagan *et al.*, 2007). Reduced travel-time prediction accuracy at regional distances results in degraded location accuracy when regional data are included (e.g., Bondár *et al.*, 2004). If regional data are to be used for seismic monitoring, then travel-time prediction error for regional phases must be reduced in order to avoid degradation of location accuracy and overall monitoring performance.

Teleseismic *P* waves work well for monitoring larger events because explosions generate large, impulsive *P* waves. *P*-wave arrival time is easily measured because the onset is not complicated by the code of other waves. Further, 1D models (e.g., Jeffreys and Bullen, 1940; Herrin *et al.* 1968; Kennett and Engdahl, 1991; Kennett *et al.*, 1995) can be used to predict teleseismic *P*-wave travel times with uncertainty of approximately 1 second, an error of less than ~0.3% of the total travel time. Accurate travel-time prediction is achievable primarily because lateral heterogeneity in the lower mantle, where most of the teleseismic *P*-wave ray path resides, is relatively weak. Also, computational error of travel times in a 1D model is negligible because model symmetry affords a quasi-analytic solution (e.g., Buland and Chapman, 1983; Crotwell *et al.*, 1999). Of particular importance to operational monitoring systems, 1D models are easy

to use. A table of travel time as a function of event–station distance and event depth can be precomputed for each seismic phase. Phase-specific travel-time tables are universally applicable when used with a correction for station elevation and Earth ellipticity (Dziewonski and Gilbert, 1976), providing fast and simple travel-time retrieval.

The *Pn* phase is generally the first regional phase to arrive, making *Pn* the regional-distance analog of the teleseismic *P* phase. The *Pn* ray path resides predominantly in the shallow (depth < 250 km) mantle. Unfortunately, a single 1D model simply cannot capture the global variability of the crust and upper-mantle structure. Crustal thickness can vary from approximately 5 km beneath oceans to more than 70 km beneath the highest mountains, and crustal and upper-mantle velocity can deviate from global averages by more than 10%. Empirically, travel-time prediction error for the *Pn* phase is 2.0–2.5 sec on average (~2% of the total travel time), and error can exceed 8 sec in some regions (e.g., Engdahl *et al.*, 1998; Flanagan *et al.*, 2007).

Both empirical- and model-based approaches have been used to improve regional travel-time prediction. Empirical methods (Schultz *et al.*, 1998; Myers and Schultz, 2000) interpolate travel-time residuals from events with known or uncommonly accurate locations (ground truth) to improve prediction accuracy. For empirical methods to be effective, ground-truth events must be well recorded at each station of the network. This condition may be met by long-standing networks and for limited geographic regions, such as former nuclear test sites. Empirical methods, however, do not provide global coverage, and travel-time prediction accuracy at new monitoring stations gradually improves as new ground-truth events are recorded.

Three-dimensional (3D) regional models show promise for improving travel-time prediction over broad areas (e.g., Johnson and Vincent, 2002; Ritzwoller *et al.*, 2003; Yang *et al.*, 2004; Morozov *et al.*, 2005; Flanagan *et al.*, 2007). Travel-time prediction using 3D models typically involves precomputing the travel time from a monitoring station to a volume of points, then, utilizing travel-time reciprocity, the travel time from any point in the volume to that station can be interpolated. Travel-time lookup volumes have been demonstrated locally and at regional distance (e.g., Lomax *et al.*, 2000; Johnson and Vincent, 2002; Flanagan *et al.*, 2007). Because explosion monitoring is concerned with near-surface events, travel-time lookups have been simplified to a map of surface-focus corrections relative to a 1D base model (e.g., Ritzwoller *et al.*, 2002; Yang *et al.*, 2004; Morozov *et al.*, 2005). Clearly, prediction error increases with event depth, and hundreds to thousands of station-phase specific correction surfaces must be managed in order to implement this approach. A collection of station-phase specific travel-time lookups has been demonstrated, but a lookup approach adds considerable expense to the cost of maintaining a monitoring system. Model updates require recomputation and (most expensively) revalidation of each station-phase file. Lastly, current models of the crust and upper mantle have been shown to produce travel-time predictions that are biased with respect to the teleseismic *P*-wave calculations (Yang *et al.*, 2004), necessitating an *ad hoc* travel-time adjustment if regional and teleseismic data are to be used together.

We are developing a model framework and a method for calculating regional seismic travel times (RSTT) that can account for the first-order effects of crust and upper-mantle heterogeneity. The model features a 3D crust, including variable Moho depth and sediment thicknesses, and laterally variable mantle structure. As we subsequently describe, a simplified model parameterization in the mantle (a linear velocity gradient) lends itself to real-time computation of *Pn* travel times, which is well suited for use in operational monitoring systems.

The RSTT model parameterization includes a global tessellation of nodes, making model coverage inherently global. While our ultimate plan is to produce a global model for universal computation of regional travel times, we first report on the RSTT model parameterization and the method of travel-time calculation for *Pn*. Secondary regional phases will be reported on in future publications. Below, we demonstrate RSTT *Pn* tomography and improvements in *Pn* travel-time prediction and location accuracy across a broad sector of the globe that includes Eurasia and North Africa (Fig. 1). This portion of the globe was chosen because of the excellent *Pn* path coverage for events with well-constrained locations. As a next step toward a the global RSTT model, we are in discussions with the U.S. Geological Survey about extending RSTT tomography to North America (Fig. 1) and subsequently incorporating the RSTT method into the National Earthquake Information Center (NEIC) processing pipeline (R. Buland, personal comm., 28 July 2009).

Methods

Model Parameterization

We represent crust and upper-mantle velocity structure using radial velocity profiles at geographically distributed nodes (Fig. 2). The nodes form a triangular tessellation that seamlessly covers the globe. Node spacing is approximately 1° for the model presented here, but node spacing may be adjusted as needed. Velocity interfaces are defined by the radial distance from the center of the Earth, which allows us to explicitly build the GRS80 ellipsoid (Moritz, 1980) into the model and obviate travel-time corrections for ellipticity.

We adopt the velocity-versus-depth profile in the crust from Pasyanos *et al.* (2004), which includes model layers for water, three types of sediments, upper crystalline crust, middle crust, and lower crust (Fig. 2; Table 1). The crustal layers overlay a mantle velocity profile that is simplified to two parameters: velocity at the Moho and a linear velocity gradient with depth. By interpolating model parameters from surrounding nodes (layer thickness, velocity, and mantle gradient), we generate a continuous model of the 3D crust and laterally varying upper mantle.

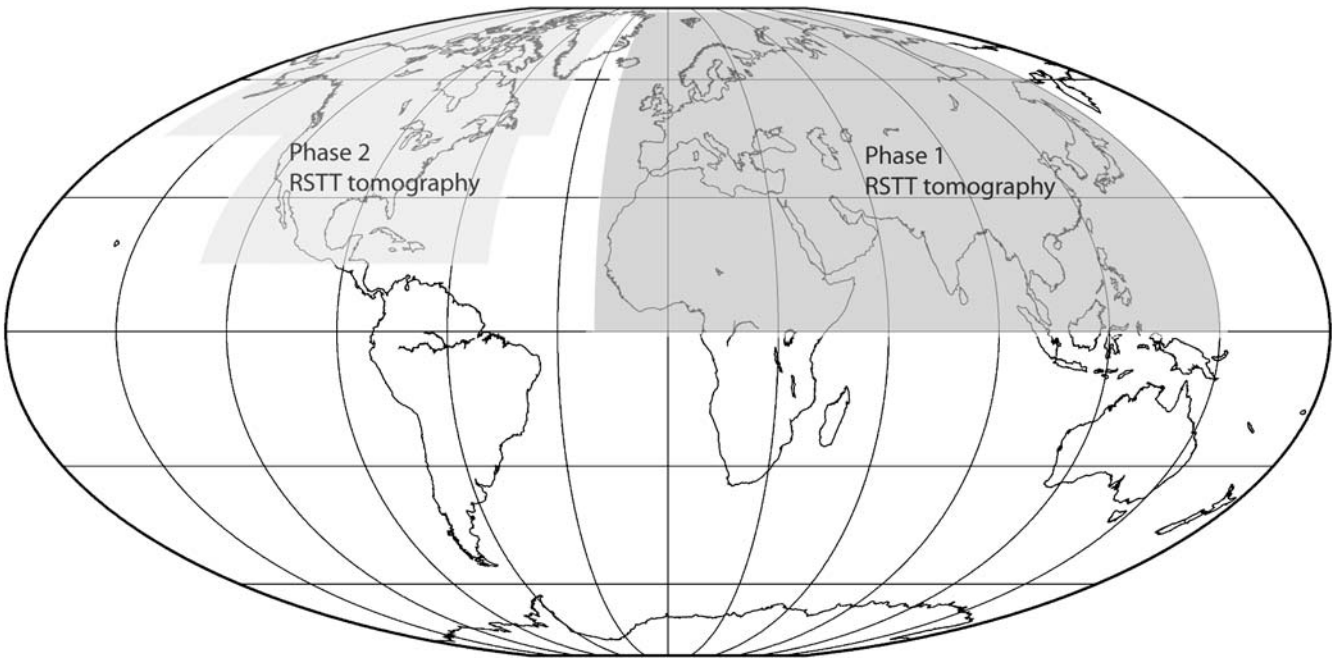

Figure 1. Phased approach for applying RSTT tomography, with the end goal of producing a global model for the universal prediction of regional phases.

Pn Travel-Time Calculation

Parameterization of upper-mantle velocity with a linear gradient facilitates an approximation for *Pn* travel time that enables real-time computation (~1 msec). Computation of *Pn* travel time at near-regional distance (< 700 km) commonly assumes that the *Pn* phase propagates as a headwave, with a ray path that follows the contour of the Moho (e.g., Hearn, 1984). The headwave assumption results in poor travel-time prediction at far-regional distance (≳700 km) because the *Pn* ray can dive appreciably into the mantle due to a positive velocity gradient with depth and Earth sphericity (e.g., Zhao and Xie, 1993; Ritzwoller *et al.*, 2003; Hearn *et al.*, 2004). To more accurately predict *Pn* at far-regional distances, Zhao (1993) and Zhao and Xie (1993) employ a constant linear velocity gradient in the upper mantle for the whole study area.

The Zhao (1993) and Zhao and Xie (1993) travel-time calculation is similar to the widely used approach of Hearn (1984), with an additional term (γ) introduced to account for diving rays (Fig. 3). The travel-time calculation is

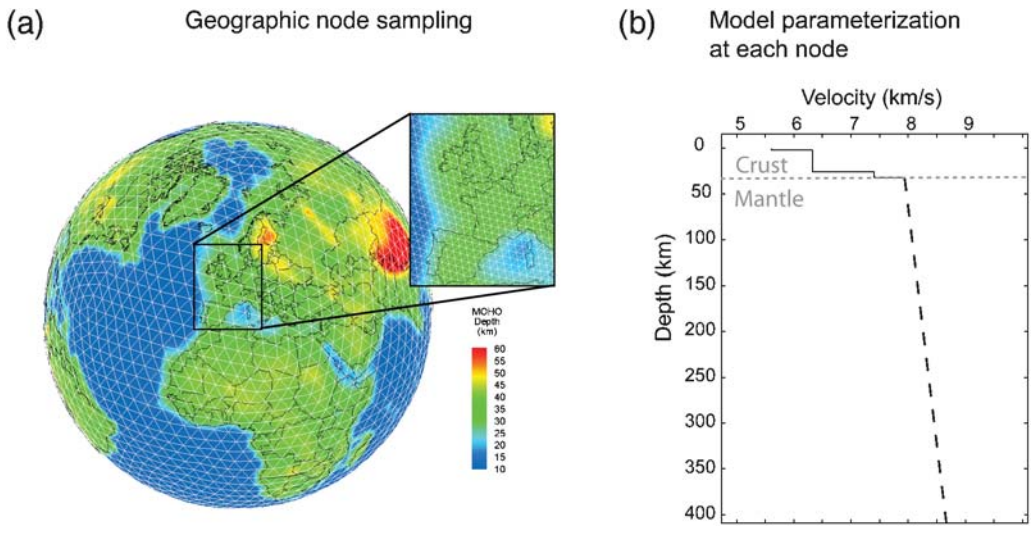

Figure 2. Global model parameterization. (a) An example tessellation with approximately 5° grid spacing. The inset shows the 1° used in this study. Color indicates Moho depth of the starting model. (b) An example velocity vs. depth profile as defined at each node. The mantle portion of the profile is specified by the velocity at the crust/mantle interface and a linear gradient.

Table 1

Definition of Model Entities Used to Construct Depth Profiles at Each Model Node*

Entity Number	Model Entity	Representation	Parameter
1	Water	Layer	Velocity
2	Sediment 1	Layer	Velocity
3	Sediment 2	Layer	Velocity
4	Sediment 3	Layer	Velocity
5	Upper crust	Layer	Velocity
6	Middle crust	Layer	Velocity
7 (Moho ⇓)	Lower crust	Layer	Velocity
8	Mantle at Moho	Half space	Velocity
9	Mantle gradient		Gradient

*Depths define the bottom of the layer. Top of a layer is implicitly the bottom of the overlaying layer. Mantle gradient is unique in that it is not a layer. The Moho is at the bottom of layer 7.

$$\mathrm{TT} = \sum_{i-1}^{N} d_i s_i + \alpha + \beta + \gamma, \tag{1}$$

where d and s are the distance and slowness (taken as 1/velocity below the Moho) in each of the i segments comprising the great-circle path between Moho pierce points near the event and station, and α and β are the crustal travel times at the receiver and source, respectively. γ is described following equation (4).

We define α as

$$\alpha = \sum_{j=1}^{M} \left[\sqrt{\frac{r_j^2}{v_j^2} - p^2} - \sqrt{\frac{r_{j+1}^2}{v_j^2} - p^2} \right], \tag{2}$$

where v and r are the velocity and radius (from the center of the Earth to the top of the layer) for the M crustal layers from the station to the Moho (r_{M+1} is the radius of the Moho), and p is the spherical ray parameter.

We similarly define β as

$$\beta = \sum_{k=1}^{L} \left[\sqrt{\frac{r_k^2}{v_k^2} - p^2} - \sqrt{\frac{r_{k+1}^2}{v_k^2} - p^2} \right], \tag{3}$$

where v and r are defined as in equation (2) for the L crustal layers from the event to the Moho.

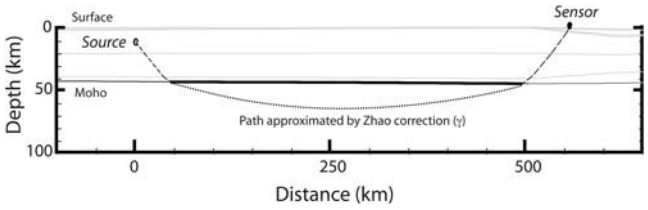

Figure 3. Cross section extracted from the laterally variable model. This example shows crustal layers (light gray), and how crustal layers can pinch out. The variable-depth Moho is also shown (thin black line). The first, second, third, and fourth terms of the *Pn* travel-time calculation (equation 1) are depicted by the bold, long dash, short dash, and dotted lines, respectively.

From Zhao (1993) and Zhao and Xie (1993),

$$\gamma = \frac{c^2 X_m^3}{24 V_0}, \tag{4}$$

where X_m is the horizontal distance traveled in the mantle, and V_0 is a regional average of mantle velocity at the Moho; and $c = g * s + 1/r$, where $1/r$ is an Earth flattening correction and r is the radius at which a ray enters and exits the linear velocity gradient, g (Helmberger, 1973; Zhao and Xie, 1993). This approximation is valid when $ch \ll 1$, where h is the bottoming depth of the ray in a linear velocity gradient.

We use a spatially varying mantle velocity gradient, c (Phillips *et al.*, 2007), and we calculate γ by averaging c along the ray track. V_0 remains an average *Pn* velocity over the whole model, which allows us to take advantage of linear tomographic inversion methods (see Tomography section). Tests find that using a global average for V_0 introduces negligible travel-time error when *Pn* velocities range from 7.5 km/sec to 8.3 km/sec.

The Zhao and Xie (1993) method is applicable to events in the crust, making the approach well suited to nuclear explosion monitoring. However, seismic location algorithms may explore the possibility that an event occurred in the mantle, necessitating a consistent method of travel-time predictions for mantle events. For an event focus in the shallow mantle,

$$\mathrm{TT} = \alpha + t_{\mathrm{mantle}}, \tag{5}$$

where α is the crustal travel time from the Moho to the station (as defined in equation 3), and t_{mantle} is the travel time in the mantle. Fundamentally, travel times for two ray paths comprise t_{mantle}. One ray has endpoints at the Moho and passes through the event (whole-mantle ray). The second ray is the subsection of the whole-mantle ray that is entirely at depths below the event (subevent path). The travel time from the event to the Moho is computed by adding (ray leaving the event downward) or subtracting (ray leaving the event upward) the subevent travel time from the whole-mantle travel time:

$$t_{\mathrm{mantle}} = \frac{1}{2}\left(\left(\sum_{i=1}^{N} d_{mi} s_{mi} + t_x - \frac{c_m^2 x_m^3}{24 V_0} \right) \pm \left(t_e - \frac{c_e^2 x_e^3}{24(V_0 + g_m z)} \right) \right). \tag{6}$$

A derivation of equation (6) is provided in the Appendix, including variable definitions and physical depictions of some variables (Fig. A1). See the Appendix for evaluation of travel-time prediction accuracy.

Tomography

Starting Model

The model development domain here is Eurasia and North Africa, which we define as the region between latitudes

0° and 90° N and longitude between 20° W and 150° E. We set velocity profiles for nodes inside the development domain based on an *a priori* geophysical model. The method for determining geophysical regions and compiling velocity information for each region is described in Pasyanos *et al.* (2004), and the starting model is an update of the Pasyanos *et al.* (2004) model for latitudes between 0° and 90° N and longitudes between 20° W and 75° E. Between longitudes 75° E and 150° E, we use an unpublished *a priori* model (Steck *et al.*, 2004). Outside of the development domain, we use a default velocity profile based on the ak135 model (Kennett *et al.*, 1995) for consistency with current monitoring practice. Expansion beyond Eurasia and North Africa does not require a change in the model parameterization itself, only modification of the velocity profile at each model node. Illustrations of the starting model (Fig. 5a,c) are presented with the tomographic model (Fig. 5b,d) for comparison.

Tomographic Formulation

The *Pn* travel time (equation 1) lends itself to a linear tomographic formulation. Because our primary objective is to improve travel-time prediction, we avoid the use of parameters that would not be part of a subsequent travel-time calculation (e.g., event and station time terms). In matrix form, the tomographic system of equations is

The tomographic equation solves for the model slowness below the Moho, s (i.e., *Pn* slowness); the square of mantle velocity gradient, c^2; and a scalar adjustment to crustal slowness, a. The formulation in equation (7) is similar to the approach presented in Phillips *et al.* (2007), with the significant difference that we use a scalar adjustment to the slowness of the crustal stack, as opposed to a time term, to account for travel-time errors in crustal legs of the *Pn* ray. The crustal legs can impart as much or more error on the travel-time prediction as the travel time in the mantle. Because our goal is to accurately predict travel times for future events using the tomographic model, it is important to fold all adjustments affecting travel time into the model rather than to absorb the error in a time term that is discarded and will not be used in subsequent travel-time prediction.

The tomographic inversion (solution to equation 7) minimizes the misfit of squared travel-time residuals that are scaled by inverse arrival-time measurement uncertainty. Regularization of the system of equations takes the form of a Laplacian damping, which minimizes the curvature of the solution. Laplacian damping is applied independently to mantle slowness, mantle gradient, and the scalar adjustment to crustal slowness. The system is solved using a conjugate gradient method (Hestenes and Siefel, 1952).

$$\begin{bmatrix} x_1^1 & \cdots & x_N^1 & \frac{x_1^1 (X_m)^3}{-24 V_0 X_m} & \cdots & \frac{x_N^1 (X_m)^3}{-24 V_0 X_m} & \sum_{p=1}^{Q} \frac{l_{1p}^1}{v_{1p}} & \cdots & \sum_{p=1}^{Q} \frac{l_{Np}^1}{v_{Np}} \\ \vdots & & & & \ddots & & & & \vdots \\ x_1^K & \cdots & x_N^K & \frac{x_1^K (X_m)^3}{-24 V_0 X_m} & \cdots & \frac{x_N^K (X_m)^3}{-24 V_0 X_m} & \sum_{p=1}^{Q} \frac{l_{1p}^K}{v_{1p}} & \cdots & \sum_{p=1}^{Q} \frac{l_{Np}^K}{v_{Np}} \\ & & & & & \text{Regularization} & & & \end{bmatrix} \times \begin{bmatrix} s_1 \\ \vdots \\ s_N \\ c_1^2 \\ \vdots \\ c_N^2 \\ a_1 \\ \vdots \\ a_N \end{bmatrix} = \begin{bmatrix} t^1 \\ \vdots \\ t^k \\ \text{Regularization} \end{bmatrix}, \quad (7)$$

where

t = travel time,
s = mantle slowness below the Moho (i.e., *Pn* slowness),
x = *Pn* distance (or weight) for each model node,
c = normalized velocity gradient, $v = v_0(1 + cz)$,
X_m = length of *Pn* ray path in the mantle,
V_0 = average *Pn* velocity,
v = velocity of a crustal layer,
k = index on K paths (travel-time observations),
p = index on Q crustal layers,
l = length of the ray path in a specified crustal layer (determined by layer thickness and ray parameter in equations 2 and 3), and
a = node-specific adjustment to the slowness of each crustal layer (crustal modifier).

Data Set

We combine bulletin data from the International Seismic Centre, U.S Geological Survey National Earthquake Information Center, and numerous regional networks across Eurasia into a reconciled database. To this database we have added tens of thousands of arrival-time measurements made at Lawrence Livermore and Los Alamos National Laboratories, as well as numerous detailed studies of event location. Epicenter accuracy for each event in the reconciled bulletin has been assessed using the network coverage criteria of Bondár *et al.* (2004). We further add nonseismic constraints based on known explosion locations, ground displacement from interferometric synthetic aperture radar (InSAR), as well as satellite imagery of man-made seismic sources. To diminish the possibility of introducing travel times for phases

that interact with velocity discontinuities at ~410 km and ~660 km, the maximum event–station distance range is set to 15°. The minimum event–station distance range is determined by the postcritical refraction for a wave interacting with the Moho. In practice, the minimum distance varies from tens of kilometers in the ocean (thin crust) to over 200 km in Tibet (thick crust).

Because the goal of this work is to produce a model for *Pn* travel-time prediction for real-time monitoring, it is important that *Pn* prediction error is unbiased relative to teleseismic *P*-wave prediction error. Previous efforts have achieved unbiased *Pn* error by using an *ad hoc* travel-time correction (Yang *et al.*, 2004). To achieve unbiased *Pn* error, we recomputed each event origin time using at least 10 *P*-wave arrivals. The hypocenter is then fixed during the tomographic procedure, which forces *Pn* prediction error to be unbiased relative to teleseismic *P*-wave error.

All picks are evaluated against an uncertainty budget that accounts for event mislocation, a global average of ak135 prediction uncertainty, and arrival-time measurement uncertainty. We map the epicenter accuracy estimates to travel-time uncertainty using the formulation of Myers (2001):

$$\sigma_{\text{tepi}} = \frac{\delta t}{\delta \Delta} \frac{\sigma_{\text{epi}}}{2}, \tag{8}$$

where σ_{tepi} (seconds) is the standard deviation of travel-time uncertainty attributable to epicenter uncertainty, σ_{epi} (km) is the standard deviation in epicenter error, and $\delta t/\delta\Delta$ is the phase slowness (sec/km). The factor of 2 accounts for random direction of event mislocation and a magnitude of mislocation that is distributed Gaussian. The total variance for a given datum is the sum of variances attributed to event location (equation 8), model-based travel-time uncertainty (e.g., Flanagan *et al.*, 2007), and arrival-time measurement uncertainty (σ^2_{meas}).

$$\sigma_{\text{datum}} = \sqrt{\sigma^2_{\text{tepi}} + \sigma^2_{\text{model}} + \sigma^2_{\text{meas}}} \tag{9}$$

In addition to data culling based on the datum-specific uncertainty budget, we also cull data based on a comparison of neighboring observations. This "local" outlier removal uses a kriging algorithm similar to the method outlined in Schultz *et al.* (1998). We gather all *Pn* residuals for a station and compute a geographic residual surface. The advantage of using the kriging method for interpolation is that we can also compute the point-specific uncertainty for residual prediction. Each residual is examined in the context of the station-specific residual and uncertainty surfaces, and only data in the 2σ bounds of the residual surface are retained. We find that outlier removal based on neighboring data produces a more consistent data set than outlier removal based on removing the tail of the global distribution.

Following removal of local outliers, we produce summary rays for each station. Arrival-time observations are again grouped by station, and residuals are plotted at the epicenter of the event. For each event, we count the number of neighboring events within 0.5° (the nominal bin size), and we order events by the count. Starting with the event having the highest count, we average residuals for all events within 0.5° to produce a summary-ray travel time and an uncertainty estimate. Events comprising the summary ray are then discarded from the event list, and the process is repeated on the event having the next highest count. This process is repeated until all events for that station are exhausted. From the ~600,000 *Pn* rays, we produce ~162,000 summary rays. The dramatic reduction reflects paths that are repeatedly

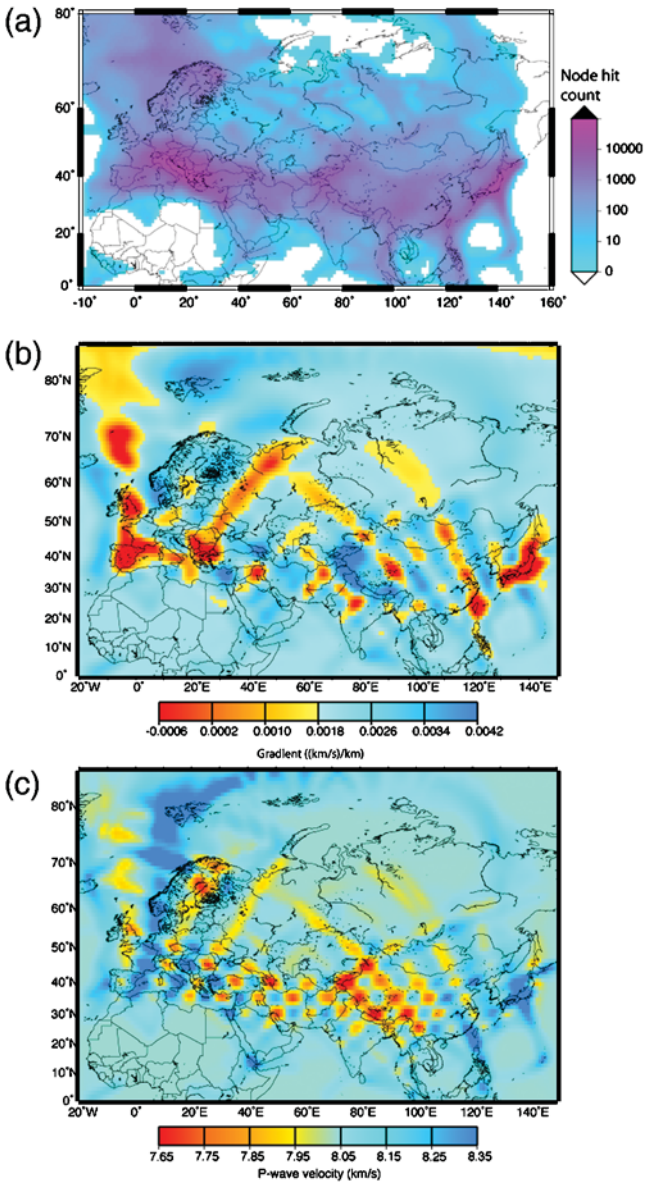

Figure 4. (a) Node hit count for *Pn* rays. Node hit count exceeds 10,000 throughout the Tethys convergence zone and Scandinavia. Hit count varies across northern Eurasia from tens of hits down to a few. North Africa and some ocean areas are devoid of data. (b) Tomographic checkerboard test for the mantle velocity gradient (~1000 km squares). (c) Tomographic checkerboard test for the mantle velocity at the Moho (~500 km squares).

sampled in areas with high seismicity. Reduction of the data set by summary rays not only reduces the number of data (and therefore reduces the computational expense of the tomography) by approximately 70%, but the average datum uncertainty is reduced from 1.73 sec to 1.28 sec. The use of summary rays also mitigates sampling redundancy, which, if left unaccounted, biases tomographic model adjustments to paths that are repeatedly sampled.

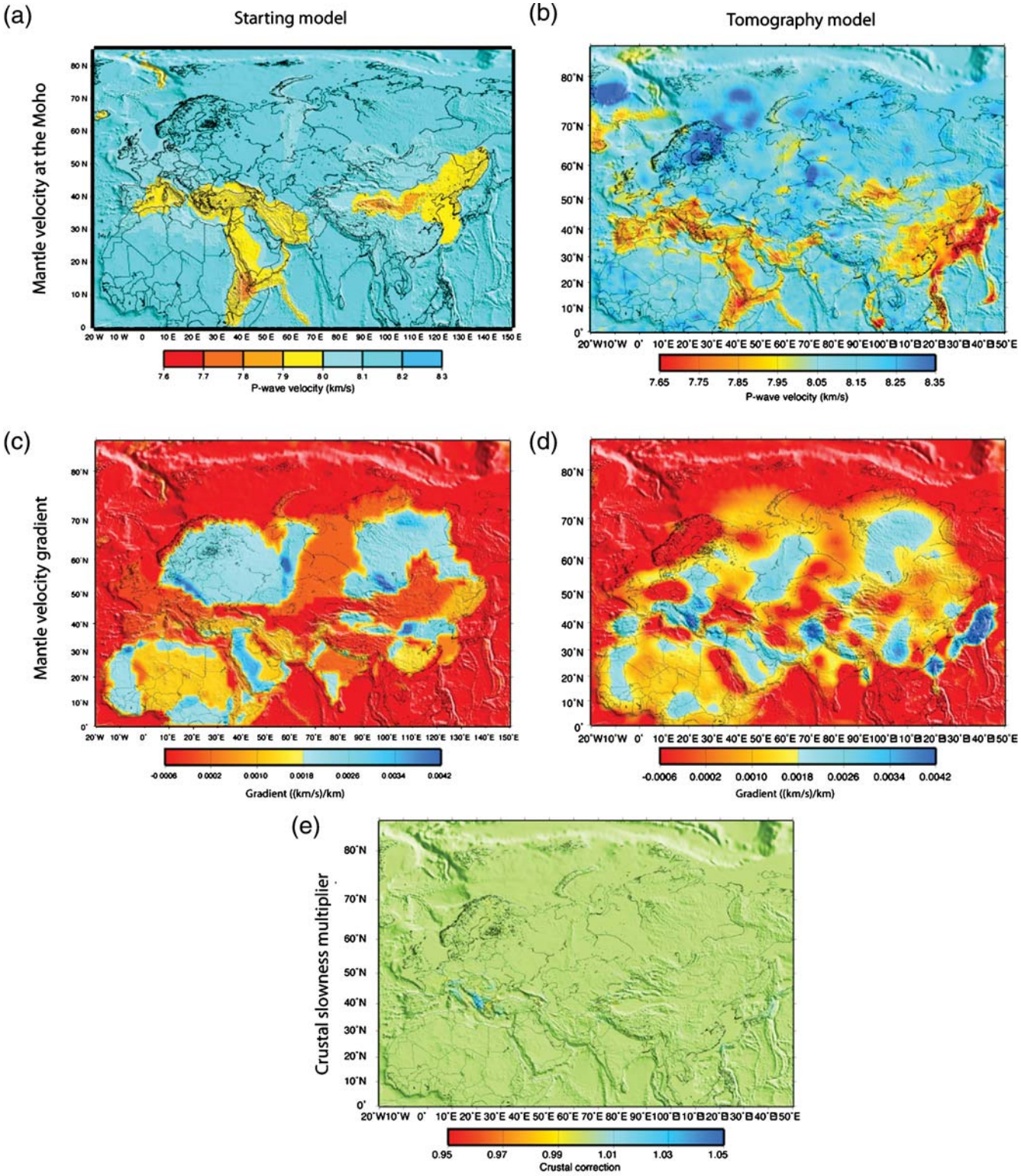

Figure 5. Comparison of starting and RSTT models. (a) Velocity below the Moho for starting model and (b) RSTT model. (c) Mantle gradient (km/sec /km) for starting model and (d) RSTT model. (e) Modification to starting model crustal slowness (*a* in equation 7).

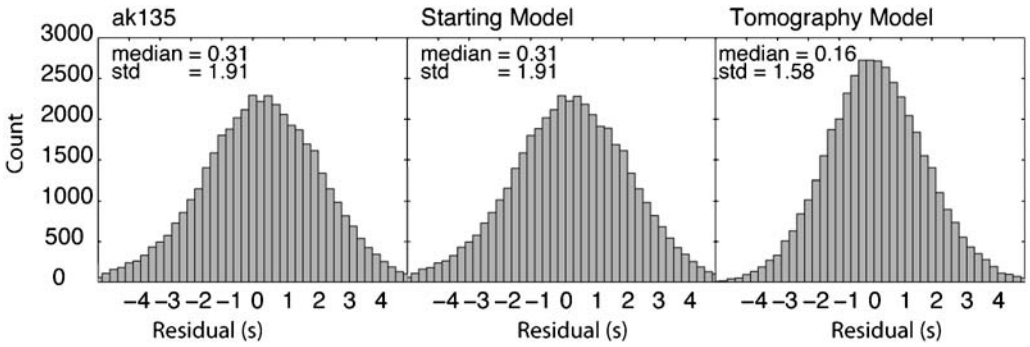

Figure 6. Travel-time residual histograms for a validation data set (not used in the tomography). The model is listed above each histogram, and summary statistics are provided in the upper left.

Data Coverage and Model Resolution

Figure 4 shows the node hit count for *Pn* summary rays throughout Eurasia, as well as the resulting tomographic "checkerboard" test for mantle-Moho velocity. The hit count is high (~10,000) throughout the Tethys collision belt (a roughly east–west band from the Pyrenees through the Himalayas). Node hit count to the north of the Tethys collision is also good, with regional bulletins and peaceful nuclear explosions in the former Soviet Union (Sultanov *et al.*, 1999) providing data coverage. South of the Tethys collision, node hit count is poorer. Some regions are not sampled by any *Pn* ray (e.g., North Africa), and the tomographic model is unaltered from the starting model in these regions.

Checkerboard resolution tests show that the model is well resolved in regions having a higher hit count. Regions with high hit count tend to have more crossing paths and a better mix of long and short paths, which are needed to resolve mantle velocity at the Moho and the velocity gradient. This result highlights the success of the anomaly recovery in regions of good data coverage and the importance of the starting model in regions with poorer data coverage.

Results

Figure 5 shows maps of the tomographic model. The general tectonic features that are present in the starting model (Fig. 5a) are also seen in the tomographic model (Fig. 5b). Low-velocity anomalies in the Mediterranean region, Red Sea Rift, and Iranian Plateau remain in the RSTT model, but the velocities are even lower. While the starting model correctly identifies the average velocity over broad regions, the RSTT model shows that structure varies appreciably within these tectonic provinces. In the Scandinavian region, mantle velocity at the Moho increases to values in excess of 8.3 km/sec. The Atlantic ridge is better defined by a sinuous low-velocity anomaly after tomography. Moving east, the starting and RSTT models are in broad agreement across the Siberian Plateau, with some small areas (e.g., immediately east of the Ural Mts.) of increased velocity. The largest difference between the starting and RSTT models is along the Pacific subduction zone. The starting model does not include low-velocity in the mantle wedge above the subducted oceanic slabs, whereas the slowest mantle *P*-wave velocities in the RSTT model are above these subducted slabs. The starting model includes low mantle velocities throughout China, whereas the RSTT model suggests that mantle velocity in eastern China is even slower than the starting model, and velocity in western China—including the Tibetan Plateau—is close to the global average. The Hindu Kush and the Tien Shan Mountains are clearly resolved to be localized areas of low mantle velocity.

Mantle velocity gradient tends to be highest in convergence zones. The tomography map of mantle gradient (Fig. 5d) shows a strong gradient along the Tethys convergence zone. Similarly, the mantle velocity gradient is high under the Pacific subduction zones, where the slow velocities of the wedge transition to the fast slab. True mantle structure in the convergence zones is clearly not as simple as the linear gradient that we image in this study, but the results presented

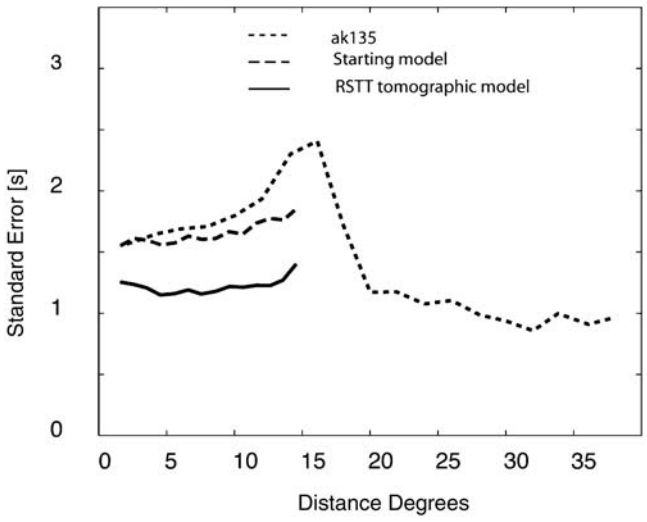

Figure 7. Travel-time error as a function of distance. The median residual in 1° distance bins is plotted for each model.

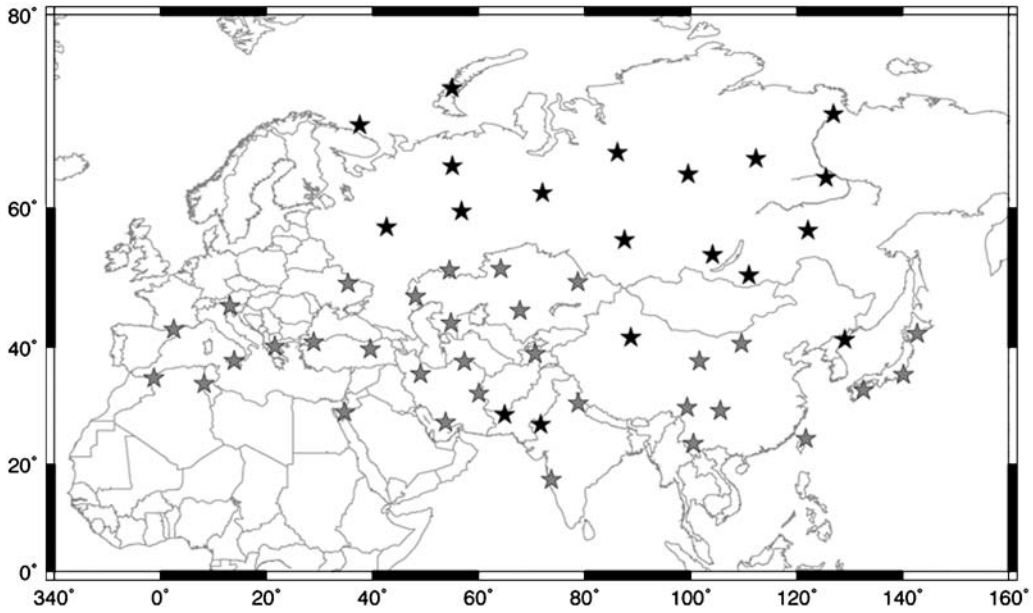

Figure 8. Validation data set used for location. Gray stars, GT5 epicenters; black stars, explosions with accurate epicenters.

here are consistent with downgoing (cold) material at the convergence zones. The linear gradient does, however, capture the effect of the structure on travel time to first order. The starting model has broad regions of strong mantle gradient across northern Eurasia, which is largely unchanged in the RSTT model. Change in the crustal modifier (a in equation 7) from the starting model is small, despite relatively light damping on the a parameters.

Improvement in Travel-Time Prediction

We leave 10% of the data out of the tomographic inversion for use in noncircular validation tests. The validation data provides sampling across Eurasia, so residual summary statistics are a good measure of expected model performance in monitoring systems. Figure 6 shows residual distributions for ak135, the starting model, and the RSTT model. Recalling

Table 2

Epicenter Error Summary Statistics

	Number of *Pn* Data							
	Median (km)				90th Percentile (km)			
Models	4	8	16	32	4	8	16	32
ak135 model	31.6	22.5	17.3	15.6	141.7	199.2	89.2	53.4
Starting model	21.7	18.1	16.8	15.0	76.0	55.2	33.3	32.8
Tomography (RSTT) model	14.4	9.3	9.3	8.2	40.4	23.3	20.9	21.1

Note: Results are for locations with station azimuthal gap less than 180°.

Table 3

Epicenter Uncertainty Ellipse Summary Statistics*

	Number of *Pn* Data							
	Median (km^2)				90th Percentile (km^2)			
Models	4	8	16	32	4	8	16	32
ak135 model	19,042	7,502	3,070	1,423	218,310	20,731	6,790	3,730
Starting model	13,900	5,704	2,738	1,432	40,947	14,129	5,114	3,962
Tomography (RSTT) model	3,297	1,765	994	478	4,843	2,549	1,490	1,018

*Note: Results are for locations with station azimuthal gap less than 180°.

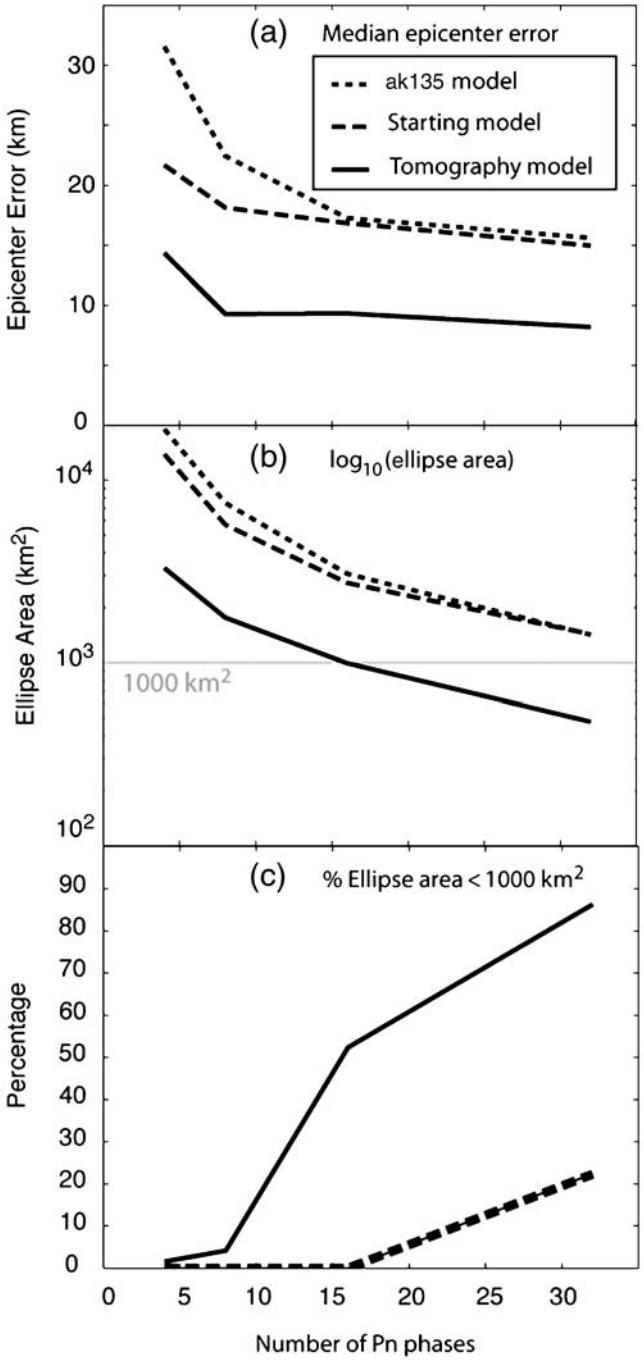

Figure 9. (a) Median epicenter error, (b) semilog plot of median ellipse area, and (c) percentage of coverage ellipses with area < 1000 km^2. In (a), (b), and (c), parameters are plotted versus number of *Pn* data used in the location. Starting model and ak135 overlap in (c).

that origin times are determined by minimizing teleseismic *P*-wave residuals relative to ak135 predictions, it is perhaps surprising that the *Pn* error for the ak135 model has a median value of 0.31 sec. The median *Pn* error for the starting model is also 0.31 sec. For the RSTT model, median *Pn* error is reduced to 0.16 sec, a 48% reduction from the ak135 model. The *Pn* residual standard deviations (mean removed) relative to the ak135, starting model, and RSTT model are 1.99 sec, 1.99 sec, and 1.58 sec, respectively.

We use an interquartile measurement to compute a robust estimate of standard error for *Pn* prediction (Fig. 7). Figure 7 includes the ak135 error vs. distance curve, as well as the curve for the starting and RSTT models. The error vs. distance curve for the starting model and ak135 are similar at near-regional distance. The ak135 uncertainty increases more rapidly with distance than does starting model uncertainty, and the starting model uncertainty is ~0.2 sec lower than ak135 at far-regional distance. The RSTT model significantly improves travel-time prediction accuracy compared to both the ak135 and starting models, with relatively stationary prediction error of approximately 1.25 sec across regional distances. We note that a nominal one-second measurement (pick) error variance was subtracted from the measured residual variance before plotting (see Flanagan *et al.*, 2007). For instance, the plotted value of 1.25 sec (variance of 1.56 sec^2) was derived from an observed residual error of 1.6 sec.

Location Tests

Figure 8 is a map of the events used in relocation tests. None of these events was used in the tomography, and each of these events is either an explosion with an accurate location or an earthquake that is surrounded by a local network (i.e., GT5 criteria of Bondár *et al.*, 2004). These events are well-distributed geographically, providing a representative sampling of location performance across the modeling region. Each event is located using *Pn* arrival times only. We use the LocOO code (Ballard, 2002), which is based on the single-event location method outlined in Jordan and Sverdrup (1981). Uncertainty ellipses were computed using the method of Evernden (1969), where coverage ellipse axes are scaled by *a priori* (input) model and pick uncertainties. For travel-time prediction uncertainties, we use the distance-dependant curves in Figure 7 and either an analyst estimate of pick uncertainty or a nominal 1-sec uncertainty. Because event depth is poorly constrained with a *Pn* data set, event depths are fixed. These events were selected partially because a large number of *Pn* arrival times are available for each event. We relocated the events using 4, 8, 16, and 32 *Pn* arrivals. Data selection was random, and we created 10 realizations of each case (number of *Pn* arrivals). Results presented subsequently are an average of the 10 realizations.

Table 2 summarizes epicenter error when the ak135, starting, and RSTT models are used for travel-time prediction in the location algorithm. The results are also summarized in Figure 9a. Figure 9a shows that the median epicenter error for the RSTT model is significantly lower than for the ak135 and starting models, regardless of the number of *Pn* arrivals. Further, the RSTT model reaches a relatively constant level of epicenter error at ~9 km with only 8 *Pn* arrivals, whereas a stable level of epicenter error at ~17 km for the ak135 and starting models is reached after 16 *Pn* arrivals are used.

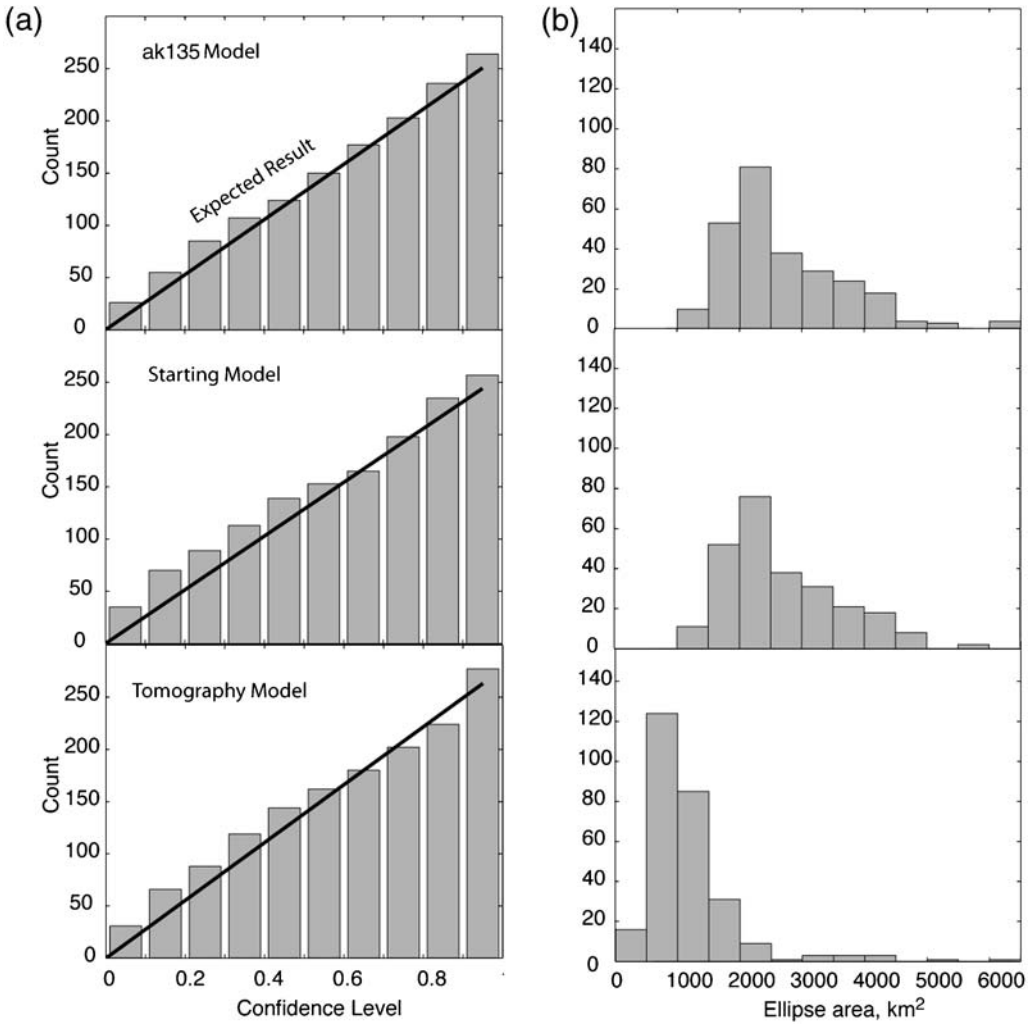

Figure 10. (a) Epicenter ellipse validation and (b) reduction in ellipse area for locations constrained with 16 *Pn* data. (a) Histograms show the number of ground-truth epicenters occurring within ellipses of varying confidence level. The expectation is that 10% of events will fall within the 10% confidence ellipse, 20% within the 20% confidence ellipse, etc. The bold lines show the expected trend of the histogram if ellipses accurately depict epicenter error. (b) Histograms show the occurrences of ellipse area for the ak135 model, starting model, and RSTT model.

Table 3 summarizes ellipse area for ak135, the starting model, and the RSTT model, when 4, 8, 16, and 32 *Pn* arrivals are used. The primary difference between the results for the ak135 and starting models is that there are fewer outliers with enormous ellipse area for the starting model than for ak135 (i.e., the tail of the distribution is shorter). Ellipses for the RSTT model are consistently smaller than for the other two models. Figure 9b is a semilog plot of median ellipse area versus the number of *Pn* phases, showing that ellipses for the RSTT model are significantly smaller than for the ak135 or the starting model. Figure 9c shows that the percentage of uncertainty ellipses with area less than 1000 km^2 is far greater for locations determined with the RSTT model. The 1000 km^2 metric is taken from the Comprehensive Nuclear Test Ban Treaty (CTBT), which allows an onsite inspection search area of 1000 km^2. When either the ak135 model or the starting model are used, the results show that with 4–8 *Pn* arrivals, none of the uncertainty ellipses are expected to be less than 1000 km^2, and even using 32 *Pn* arrivals results in only ~23% of uncertainty ellipses with area less than 1000 km^2. Using the RSTT model, it is possible to achieve the 1000 km^2 goal with only 4 *Pn* arrivals, although the network configuration must be ideal. With 16 *Pn* arrivals, approximately one-half of the events meet the 1000 km^2 goal; and, with 32 *Pn* arrivals, ~88% of ellipses meet the 1000 km^2 goal.

Figure 10a shows that coverage ellipses are representative of true location error when the assessments of model error (Fig. 7) are input to the location algorithm. In other words, the expected number of ground-truth events occurs inside the ellipses of varying confidence level. Figure 10b shows the reduction in error ellipse size for the case with 16 *Pn* arrivals.

Combining *Pn* and *P* Data

While low-magnitude events are expected to record more reliably at regional distance than at teleseismic distance, a

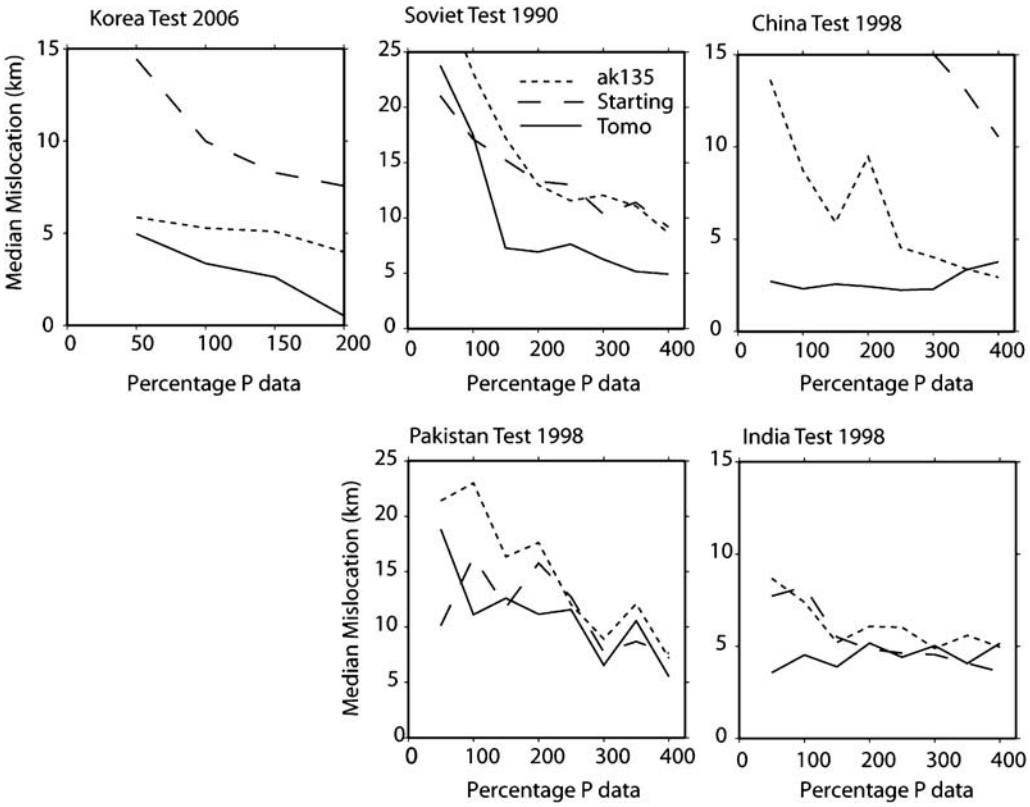

Figure 11. Epicenter accuracy with mixed *Pn*/*P* data sets. All *Pn* arrivals are used. Each plot shows the influence of adding (teleseismic) *P* arrivals and using the ak135 model to predict *P* travel times. The abscissa is computed as the number of *P* arrivals divided by the number of *Pn* arrivals multiplied by 100. Median epicenter error for 10 realizations is plotted.

small number of teleseismic (*P*) recordings may be expected even for events between magnitudes 3 and 4. For a small event, it is important to include all available data to achieve a network with the smallest possible gap in event–station azimuthal coverage. Therefore, we test epicenter accuracy when both *Pn* and *P* data are used to determine the location. In these tests, ak135 is used for *P*-wave travel-time calculations, and ak135, the starting model, and the RSTT model are each tested for *Pn* travel-time calculations.

For each of the nuclear explosions in the test data set, we use all available *Pn* data. We then add *P*-wave arrivals into the location data set. For each test case, the number of *P* arrivals is varied from 50% to 400% of the number of *Pn* arrivals or until *P*-wave data are exhausted. In each test case, we present the median epicenter error for 10 random realizations of the *P*-wave data set. Figure 11 shows that when the RSTT model is used for *Pn* travel-time predictions and the ak135 model is used for *P* predictions, epicenter estimates are measurably more accurate than cases in which either ak135 or the starting model is used for *Pn* travel-time predictions. In most cases, epicenter accuracy tends to converge as more *P* data are used because the location solution is dominated by ak135 predictions of *P*-wave travel times. The exceptions are the 2006 Korean nuclear test and the 1990 nuclear test in the Former Soviet Union event. For the Korean event, epicenter error becomes exceedingly small for the RSTT model (~1 km), and, for the Soviet event, regional travel-time errors are large enough that the locations are significantly biased even when large numbers of teleseismic data are used. In all cases in which *Pn* data outnumber or are equal in number to teleseismic data, epicenter accuracy for the RSTT model is equal to or better than epicenter accuracy when the ak135 model is used for *Pn* travel-time prediction.

Conclusions

Reduction of seismic monitoring thresholds requires the use of regional seismic data to constrain event locations. One-dimensional (radially symmetric) models that are almost universally used in real-time monitoring cannot account for the geologic complexity of the crust and upper mantle. We develop a regional seismic travel-time (RSTT) model and method to account for the first-order effects of crust and upper-mantle structure on regional travel times. The model parameterization is a global tessellation with node spacing of approximately 1°, with a velocity vs. depth profile at each node. Layer depths and velocities are interpolated to generate a 3D crustal model, overlaying laterally varying velocity in the upper mantle. Velocity profiles in the mantle include a velocity at the Moho and a linear gradient as a function of depth. The linear gradient

parameterization allows application of an analytical approximation that accounts for a *Pn* ray that dives below the Moho into a linear velocity gradient (Zhao and Xie, 1993; Phillips *et al.*, 2007). Because of this approximation, *Pn* travel times can be computed in approximately 1 msec, which is highly desirable for operational monitoring systems.

We adapt tomographic methods to the RSTT model parameterization and use a data set of approximately 600,000 *Pn* arrivals to improve travel-time prediction accuracy across Eurasia and North Africa. Tests show that RSTT *Pn* travel-time prediction accuracy is improved to approximately that of the teleseismic *P* wave, which is the benchmark phase in seismic monitoring. We confirm that the reduction in travel-time prediction error also improves location accuracy (Fig. 9). Using 16 *Pn* arrivals, epicenter error is improved from a median value of 17.3 km with the ak135 model to 9.3 km with the RSTT model. The area of epicenter uncertainty ellipses is reduced from a median value of 3070 km^2 using the ak135 model to 994 km^2 using the RSTT model (Fig. 10). Of particular note, Figure 9c shows that few epicenter uncertainty ellipses are expected to meet the 1000 km^2 goal when either the ak135 model or the starting model is used. Using the RSTT model, it is possible to achieve the 1000 km^2 goal with only 4 *Pn* arrivals, although the network configuration must be ideal. Using 32 *Pn* arrivals, ~88% of ellipses meet the 1000 km^2 goal.

The RSTT model improves the *Pn* travel-time prediction accuracy to a level comparable to that of teleseismic *P*, which is the primary phase used in global monitoring. As a result, the RSTT approach enables the use of regional *Pn* arrival times in seismic monitoring systems without degrading location performance. RSTT is presented as a first step beyond the use of a 1D base model in operational monitoring systems. While the base model provides the primary travel-time calculation, travel-time corrections that are based on fully 3D models or empirical travel times can and should be used to further improve prediction accuracy. While the RSTT model is global in extent, the crucial tomographic optimization is currently limited to Eurasia and North Africa; however, we plan to apply RSTT tomography to North America and eventually to the globe. Last, we have extended RSTT travel-time calculation to *Sn*, *Pg*, and *Lg* phases, and we will report on the travel-time calculation and model development for computation of these later phases in a future publication.

Data and Resources

Most of the arrival-time measurements used in this study can be obtained from the International Seismic Centre (ISC). Bulletin arrival times include the Earthquake Data Report catalog (http://earthquake.usgs.gov/regional/neic), the ISC catalog (http://www.isc.ac.uk), the Reviewed Event Bulletin catalog prior to 2002 (http://www.pidc.org), the Engdahl–van der Hilst–Buland (EHB) catalog (ftp://ciei.colorado.edu/pub/user/engdahl/EHB), and the Finnish seismic bulletin produced by the University of Helsinki (http://www.seismo.helsinki.fi/english/research/projects/parametersEng.html), all of which are publicly available.

Additional arrival-time measurements were made by researchers at the Air Force Technical Applications Center, Lawrence Livermore National Laboratory (LLNL), and Los Alamos National Laboratory (LANL); these measurements are not presently available to the public. Measurements made at LLNL and LANL were made using waveform data obtained through the Incorporated Research Institutes in Seismology Data Management Center (IRIS-DMC) at www.iris.edu, the U.S. National Data Center (USNDC) at www.tt.aftac.gov, GEOSCOPE at geoscope.ipgp.jussieu.fr, International Institute of Earthquake Engineering and Seismology (IIEES) at www.iiees.ac.ir, GEOFON at geofon.gfz-potsdam.de, and MEDNET at mednet.rm.ingv.it. Other data were obtained directly from networks in Azerbaijan, Georgia, Israel, Jordan, Kazakhstan, Kuwait, Oman, Saudi Arabia, Turkey, and United Arab Emirates. Plots were made using Generic Mapping Tools (GMT), version 4.2.0 (Wessel and Smith, 1998; available at www.soest.hawaii.edu/gmt).

Acknowledgments

We thank the Office of Nuclear Detonation Detection (NA-222) within the National Nuclear Security Administration for funding this effort. David Russell provided critical guidance in the formative stages of the RSTT project. Leslie Casey provided useful comments and suggestions. Jiakang Xie and an anonymous reviewer helped to improve the manuscript. This work was performed under the auspices of the U.S. Department of Energy by University of California Lawrence Livermore National Laboratory under contract no. DE-AC52-07NA27344. This article is document LLNL-JRNL-411605.

References

Ballard, S. (2002). Seismic event location using Levenberg–Marquardt least squares inversion, *Sandia National Laboratories Report*, SAND2002-3083, 25 pp.

Bondár, I., S. Myers, E. R. Engdahl, and E. Bergman (2004). Epicenter accuracy based on seismic network criteria, *Geophys. J. Int.* **156,** no. 3, 483–496.

Buland, R., and C. Chapman (1983). The computation of seismic travel times, *Bull. Seismol. Soc. Am.* **73,** 1271–1302.

Crotwell, H. P., T. J. Owens, and J. Ritsema (1999). The TauP ToolKit: Flexible seismic travel-time and raypath utilities, *Seismol. Res. Lett.* **70,** 154–160.

Dziewonski, A., and F. Gilbert (1976). The effect of small, aspherical perturbations on travel time and a re-examination of the corrections for ellipticity, *Geophys. J. R. Astr. Soc.* **44,** 7–17.

Engdahl, E. R., R. van der Hilst, and R. Buland (1998). Global teleseismic earthquake relocation with improved travel times and procedures for depth determination, *Bull. Seismol. Soc. Am.* **88,** 722–743.

Evernden, J. F. (1969). Precision of epicenters obtained by small numbers of world wide stations, *Bull. Seismol. Soc. Am.* **59,** 1365–1398.

Flanagan, M. P., S. C. Myers, and K. D. Koper (2007). Regional travel-time uncertainty and seismic location improvement using a three-dimensional *a priori* velocity model, *Bull. Seismol. Soc. Am.* **97,** 804–825.

Hearn, T. M. (1984). *Pn* travel times in southern California, *J. Geophys. Res.* **89,** 1843–1855.

Hearn, T. M., S. Wang, J. F. Ni, Z. Xu, Y. Yu, and X. Zhang (2004). Uppermost mantle velocities beneath China and surrounding regions, *J. Geophys. Res.* **109,** B11301, doi 10.1029/2003JB002874.

Helmberger, D. V. (1973). Numerical seismograms of long-period body waves from seventeen to forty degrees, *Bull. Seismol. Soc. Am.* **63,** 633–646.

Herrin, E., W. Tucker, J. Taggart, D. Gordon, and J. Lobell (1968). Estimation of surface focus *P* travel times, *Bull. Seismol. Soc. Am.* **58,** 1273–1291.

Hestenes, M. R., and E. Stiefel (1952). Methods of conjugate gradients for solving linear systems, *J. Res. Natl. Bur. Stand.* **49,** no. 6, 409–436.

Jeffreys, H., and K. E. Bullen (1940). *Seismological Tables*, British Association for the Advancement of Science, London.

Johnson, M., and C. Vincent (2002). Development and testing of a 3-D velocity model for improved event location: A case study the India–Pakistan region, *Bull. Seismol. Soc. Amer.* **92,** 2893–2910.

Jordan, T. H., and K. A. Sverdrup (1981). Teleseismic location techniques and their application to earthquake clusters in the south-central Pacific, *Bull. Seismol. Soc. Am.* **71,** 1105–1130.

Kennett, B. L. N., and E. R. Engdahl (1991). Travel times for global earthquake reference location and phase identification, *Geophys. J. Int.* **105,** 429–465.

Kennett, B. J. N., E. R. Engdahl, and R. Buland (1995). Constraints on seismic velocities in the Earth from travel times, *Geophys. J. Int* **122,** 108–124.

Lomax, A., J. Virieux, P. Volant, and C. Berge (2000). Probabilistic earthquake location in 3-D and layered models: Introduction of a Metropolis–Gibbs method and comparison with linear locations, in *Advances in Seismic Event Location*, C. H. Thurber and N. Rabinowitz (Editors), Kluwer, Amsterdam, 101–134.

Moritz, H. (1980). Geodetic reference system 1980, *Bull. Geodesique Paris* **54,** no. 3, 5 pp.

Morozov, I. B., E. A. Morozova, S. B. Smithson, P. G. Richards, V. I. Khalturin, and L. N. Solodilov (2005). 3-D First-arrival regional calibration model of northern Eurasia, *Bull. Seismol. Soc. Amer.* **95,** 1535–1560, doi 10.1785/0120040087.

Myers, S. C. (2001). Methods of travel-time residual declustering for the Knowledge Base Calibration and Integration Tool (KBCIT), *Lawrence Livermore National Laboratory Report*, UCRL-ID-142521, 14 pp.

Myers, S. C., and C. A. Schultz (2000). Improving sparse network seismic location with Bayesian kriging and teleseismically constrained calibration events, *Bull. Seismol. Soc. Am.* **90,** 199–211.

Pasyanos, M. E., W. R. Walter, M. P. Flanagan, P. Goldstein, and J. Bhattacharyya (2004). Building and testing an *a priori* geophysical model for western Eurasia and North Africa, *Pure Appl. Geophys.* **161,** 235–281.

Phillips, W. S., M. L. Begnaud, C. A. Rowe, L. K. Steck, S. C. Myers, M. E. Pasyanos, and S. Ballard (2007). Accounting for lateral variations of the upper mantle gradient in *Pn* tomography studies, *Geophys. Res. Lett.* **34,** L14312, doi 10.1029/2007GL029338.

Ritzwoller, M. H., M. P. Barmin, A. Villasenor, A. L. Levshin, and E. R. Engdahl (2002). *Pn* and *Sn* tomography across Eurasia to improve regional seismic locations, *Tectonophysics* **358,** 39–55.

Ritzwoller, M. H., N. M. Shapiro, A. Levshin, E. A. Bergman, and E. R. Engdahl (2003). The ability of a global 3-D model to locate regional events, *J. Geophys. Res.* **108,** 2353, doi 10.1029/2002JB002167.

Schultz, C. A., S. C. Myers, J. Hipp, and C. Young (1998). Nonstationary Bayesian kriging: A predictive technique to generate corrections for detection, location, and discrimination, *Bull. Seismol. Soc. Am.* **88,** 1275–1288.

Steck, L. K., C. A. Rowe, M. L. Begnaud, W. S. Phillips, V. L. Gee, and A. A. Velasco (2004). Advancing seismic event location through difference constraints and three-dimensional models, paper presented at *26th Seismic Research Review—Trends in Nuclear Explosion Monitoring*, Orlando, Florida, 21–23 September 2004.

Sultanov, D. D, J. R. Murphy, and K. D. Rubinstein (1999). A seismic source summary for Soviet peaceful nuclear explosions, *Bull. Seismol. Soc. Am.* **89,** 640–647.

Yang, X., I. Bondár, J. Bhattacharyya, M. Ritzwoller, N. Shapiro, M. Antolik, G. Ekström, H. Israelsson, and K. McLaughlin (2004). Validation of regional and teleseismic travel-time models by relocating ground-truth events, *Bull. Seismol. Soc. Amer.* **94,** 897–919.

Zhao, L.-S. (1993). Lateral variations and azimuthal isotropy of *Pn* velocities beneath Basin and Range province, *Jour. Geophys. Res.* **98,** 22,109–22,122.

Zhao, L.-S., and J. Xie (1993). Lateral variations in compressional velocities beneath the Tibetan Plateau from *Pn* travel time tomography, *Geophys. J. Int.* **115,** 1070–1084.

Appendix

Calculating Travel Times for Mantle Events

Zhao and Xie (1993) and Zhao (1993) provide a derivation for *Pn* travel-time approximation that we use in equations (1) and (4) for events in the crust. We extend the approximation for events originating in the mantle. Figure A1 shows that extending the Zhao and Xie (1993) approximation to an event in the mantle involves manipulation of two constituent ray paths. The first constituent ray starts at the Moho and travels downward, passing through the event, and ends at the recording station (whole-path ray). The travel time for the portion of the whole-path ray in the mantle (whole-mantle ray) is calculated directly from Zhao and Xie (1993). The second constituent ray is the portion of the whole-path ray that is

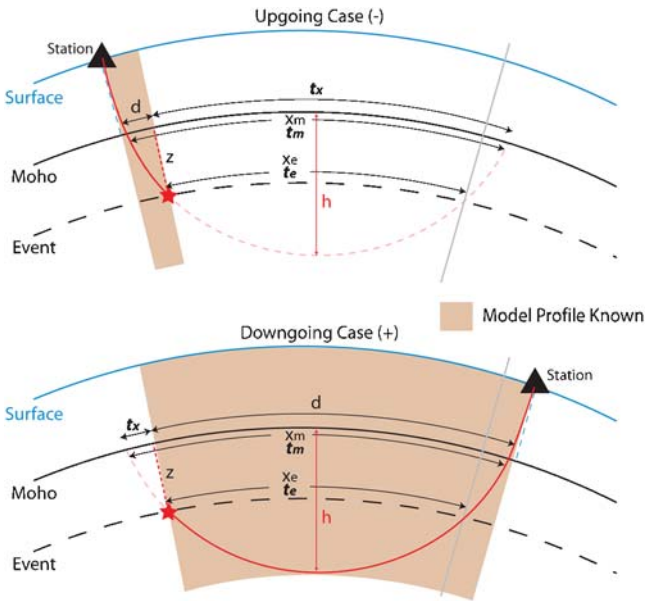

Figure A1 Geometry and variable definition extending the Zhao and Xie (1993) formulation to events in the shallow mantle. Red star, event location; triangle, station location; muted dashed red line, theoretical projected portion of the ray path. Note that horizontal distances are evaluated in a flat earth, and Appendix equations correct for Earth sphericity.

entirely below the event (subevent path). Using the travel times for the whole path and the subevent ray, we can compute the travel time for a mantle-focus event. The difficulty lies in specifying the whole-path and subevent rays.

Following Zhao and Xie (1993) and Zhao (1993), the travel time for the whole-mantle ray is

$$t_{wm} = t_m + \gamma_m = t_m - \frac{c_m^2 x_m^3}{24 V_m}, \tag{A1}$$

where t is travel time, γ is the gradient portion of the travel time (always negative), c is the normalized gradient, x is the horizontal distance, V is velocity, the m subscript signifies evaluation at or along the Moho, and the subscript wm signifies whole mantle.

The travel time for the subevent ray is

$$t_{se} = t_e + \gamma_e = t_e - \frac{c_e^2 x_e^3}{24 V_e} = t_e - \frac{c_e^2 x_e^3}{24(V_m + g_m z)}, \tag{A2}$$

where the subscript e signifies evaluation at or along the depth of the event, and the subscript se signifies subevent. All other terms are as defined in equation (A1).

From the geometry in Figure A1, the travel time from the event to the Moho pierce point beneath the station (the desired quantity) can be computed as a combination of t_{wm} and t_{se}:

$$t_{\text{mantle}} = (t_{wm} \pm t_{se})/2, \tag{A3}$$

where $\pm$ depends on whether the ray leaves the event upwards ($-$) or downwards ($+$).

Determining the Whole-Mantle Ray

In order to use equation (A3), we must find the whole-mantle ray. We first define the horizontal distance traveled by the whole-mantle ray, x_m. In a linear velocity gradient, the bottoming depth of the ray, h, and x_m are uniquely related. From Figure A1, the distance measured along the Moho from the event to the point where the ray pierces the Moho, d, is

$$d = \left(x_m \pm \frac{r_m x_e}{(r_m - z)} \right)/2, \tag{A4}$$

where x_e is the horizontal distance of the subevent path. The $\pm$ indicates when the ray is upgoing ($-$) or downgoing ($+$), r_m is the radius from the center of the Earth to the Moho at the event, and z is the depth of the event below the Moho. Zhao (1993) gives us

$$x_m = (2/c_m)\sqrt{(1 + c_m h)^2 - 1} \tag{A5}$$

and

$$x_e = (2/c_e)\sqrt{(1 + c_e(h - z))^2 - 1}. \tag{A6}$$

We determine h by substituting equations (A5) and (A6) into equation (A4) (simplifying $r = r_m/(r_m - z)$) and minimizing the difference between the distance (d) computed by equation (A1). In practice, we minimize $\log_{10}$ of the squared difference using Brent's method:

$$\log\left(\left(\sqrt{(1 + c_m h)^2 - 1} - r\frac{c_m}{c_e}\sqrt{(1 + c_e(h - z))^2 - 1} - dc_m \right)^2 \right) (\text{up-going}), \tag{A7}$$

$$\log\left(\left(\sqrt{(1 + c_m h)^2 - 1} + r\frac{c_m}{c_e} \times \sqrt{(1 + c_e(h - z))^2 - 1} - dc_m \right)^2 \right) (\text{down-going}), \tag{A8}$$

and use the misfit to determine whether the ray is upgoing or downgoing. The values for x_m and x_e, which depend on the Moho pierce point, are recalculated using an updated ray parameter for the turning-point depth (h), and the procedure is iterated to convergence.

Computing Normalized Gradient and Travel Time

Once the values of x_m and x_e are determined, they can be substituted into equations (A1) and (A2) to compute the travel time for the whole-mantle ray and the subevent ray, and we can use equation (A3) to compute the mantle portion of the travel time for the event of interest. The following clarifies details of the calculation. The travel time along the Moho is simply a sum of the slowness multiplied by the incremental distances as in equation (1), with an additional component for the Moho travel-time beyond the source-receiver distance (t_x; see Fig. A1):

$$t_x = \frac{x_m - d}{V_m}. \tag{A9}$$

A headwave travel time along the event depth path is determined using the path-averaged velocity at depth z:

$$t_e = \frac{x_e}{V_m + g_m z}. \tag{A10}$$

The normalized gradient c in equations (A1) and (A2) vary slightly, depending on whether the purpose of the

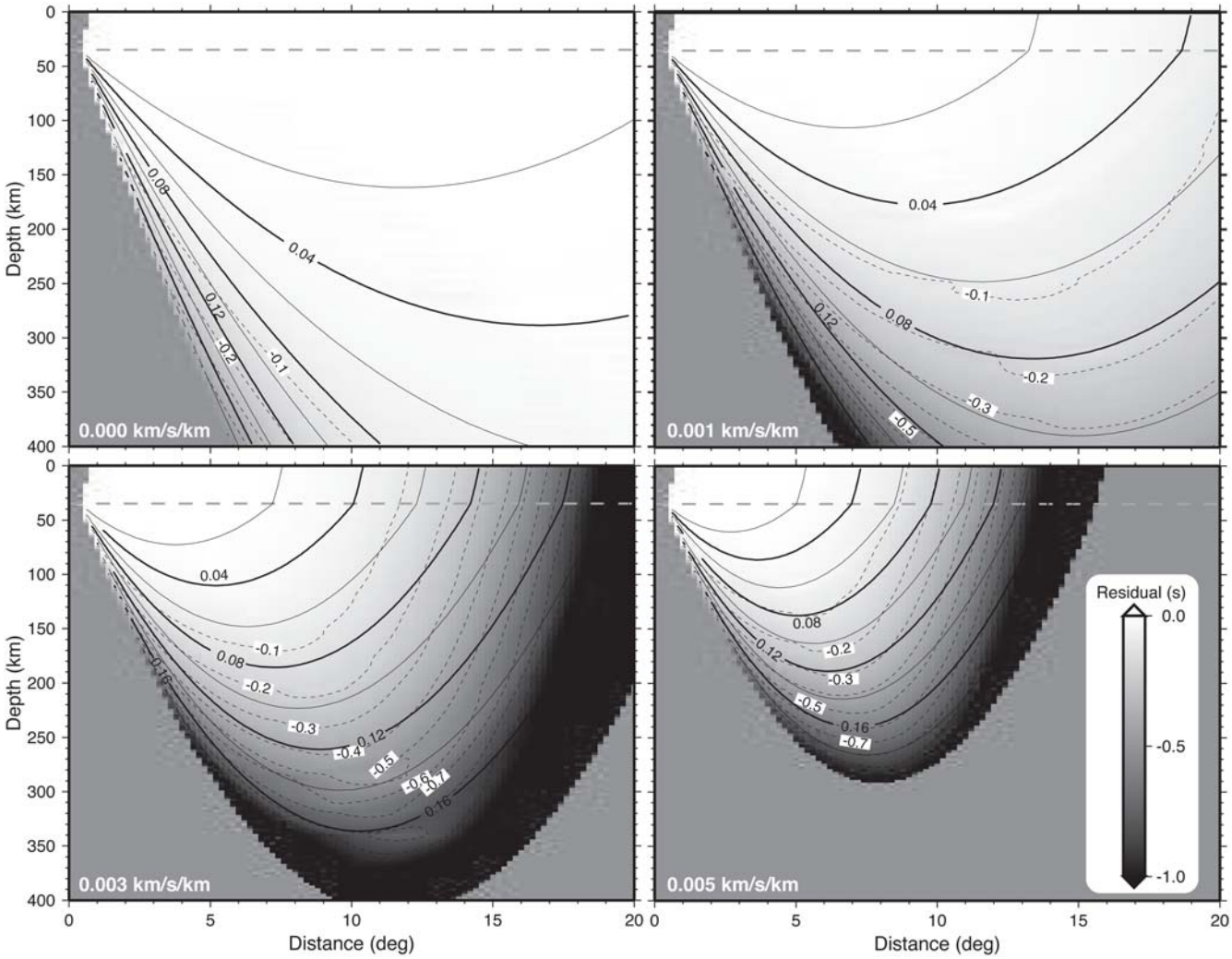

Figure A2 Travel-time differences between equation (A15) and the TauP toolkit (Crotwell *et al.*, 1999) for varying mantle-gradient values. The ak135 crust and velocity at the Moho were used in each model. Only the gradient is varied. The solid lines are contours of equal *ch* values (see text). Dotted contour lines are of equal residual value, with an interval of 0.1 sec.

calculation is to find the turning-point depth (h) or the gradient portions of the travel times. When determining h in equations (A4)–(A8), the normalized gradient uses the path-averaged velocity

$$c_m = \frac{g_m}{V_m} + \frac{1}{r_m}, \tag{A11}$$

$$c_e = \frac{g_m}{V_e} + \frac{1}{r_e} = \frac{g_m}{V_m + g_m z} + \frac{1}{r_e}. \tag{A12}$$

When calculating the gradient portions of the travel times in equations (A1)–(A3) and (A11)–(A12), we substitute a regional average of the Moho velocity V_0 for V_m in order to keep travel times consistent with crustal events and the tomography:

$$c_m = \frac{g_m}{V_0} + \frac{1}{r_m}, \tag{A13}$$

$$c_e = \frac{g_m}{V_0 + g_m z} + \frac{1}{r_e}. \tag{A14}$$

The full travel time for a mantle event becomes

$$t_{\text{mantle}} = \frac{1}{2}\left(\left(\sum_{i=1}^{N} d_{mi} s_{mi} + t_x - \frac{c_m^2 x_m^3}{24 V_0}\right) \pm \left(t_e - \frac{c_e^2 x_e^3}{24(V_0 + g_m z)}\right)\right), \tag{A15}$$

which can also be separated into headwave and gradient components:

$$t_{\text{head}} = \frac{1}{2}\left(\sum_{i=1}^{N} d_{mi}s_{mi} + t_x \pm t_e\right)$$
$$= \frac{1}{2}\left(\sum_{i=1}^{N} d_{mi}s_{mi} + \frac{x_m - d}{V_m} \pm \frac{x_e}{V_m + g_m z}\right), \quad \text{(A16)}$$

$$t_{\text{gradient}} = -\frac{1}{48}\left(\frac{c_m^2 x_m^3}{V_0} \pm \frac{c_e^2 x_e^3}{V_0 + g_m z}\right). \quad \text{(A17)}$$

Validity of the Zhao and Xie (1993) Approximation

Zhao (1993) assumes that the product of the normalized mantle velocity gradient (c) and the bottoming depth of the ray traveling in the linear velocity gradient (h) is much less than 1 (i.e., $ch \ll 1$). We test the accuracy of the calculation using a model with the ak135 crust and Moho velocity (Kennett *et al.*, 1995), underlain by a mantle with a linear velocity gradient. Test cases include gradients of 0.000, 0.001, 0.003, and 0.005 km/sec/km (Fig. A2). As expected, the error approximately follows the contour of ch. The goal of a computational error of less than 0.2 sec is approximately met when $ch < 0.12$. We note that tomographic procedures will force the travel time to agree with observations and therefore meet the goal of this project, which is improved travel-time predictions for monitoring. We caution that ch should be carefully assessed before model velocities are interpreted.

Lawrence Livermore National Laboratory
L-046
Box 808
7000 East Ave.
Livermore, California 94550
(S.C.M., M.E.P., A.L.R.)

Geophysics Group, EES-17, MS F665
Los Alamos National Laboratory
P.O. Box 1663
Los Alamos, New Mexico 87545
(M.L.B., W.S.P., C.A.R.)

Sandia National Laboratories
P.O. Box 5800
Mail Stop 0401
Albuquerque, New Mexico 87185-0401
(S.B.)

Quantum Technology Sciences, Inc.
1980 N. Atlantic Ave., Suite 930
Cocoa Beach, Florida 32930
(M.S.A., K.D.H.)

Air Force Technical Applications Center
1030 South Highway A1A
Patrick Air Force Base, Florida 32925
(J.J.D., G.S.W.)

Manuscript received 29 July 2009